Chemical Science

ROYAL SOCIETY OF CHEMISTRY

EDGE ARTICLE

View Article Online
View Journal

Cite this: DOI: 10.1039/d6sc00912c

All publication charges for this article have been paid for by the Royal Society of Chemistry

Spin-regulated d–p hybridization enables high energy density and wide temperature operation of $Na_3V_2(PO_4)_2O_2F$-type cathodes for sodium-ion batteries

Qiang Fu,[a] Qin He,[a] Fangxiang Song,[a] Xianquan Ao,*[ab] Hanxiao Liu,[c] Yang Cao,[ab] Rong Li,*[a] Keliang Wang,[d] Jing Li,[d] Cuiqin Li[a] and Yao Xiao*[c]

As a member of the sodium superionic conductor (NASICON) family, $Na_3V_2(PO_4)_2O_2F$ (NVPOF) has attracted tremendous research interest owing to its high operating voltage and excellent structural stability. It is well established that NVPOF cathodes are electron-ion mixed conductors. However, improving electron or ionic conductivity *via* a single approach fails to effectively enhance the rapid sodium storage capability, which impedes their practical application in sodium-ion batteries. Herein, the electronic and ionic conductivities were enhanced through a transition-metal/fluorine dual-doping method. The introduction of transition metals with different spin states adjusted the spacing between the V $3d_{xz}$–O $2p_x$ bond and the Fermi level, thereby improving the material's intrinsic conductivity. Meanwhile, the introduction of F atoms effectively optimized the diffusion kinetics of Na^+. In particular, $Na_3(VO)_{1.9}Fe_{0.1}(PO_4)_2F_{1.1}$ (NVPOF–Fe) is obtained by dual-doping with high-spin Fe^{3+}/F^-. It has considerable specific capacity and power density at 100C (80 mA h g^{-1}, 245 Wh kg^{-1}) and retains 90.6% capacity after 2500 cycles at 20C. The assembled NVPOF–Fe||hard-carbon full cell exhibits excellent capacity and cycling stability at −20 °C, 25 °C, and 45 °C, respectively. This work provides a new paradigm for the development of advanced sodium-ion battery cathodes.

Received 2nd February 2026
Accepted 3rd March 2026

DOI: 10.1039/d6sc00912c

rsc.li/chemical-science

Introduction

Industry 4.0 introduces digitalization and intelligent manufacturing, which further increase energy demand.[1] Electrical energy storage (EES) systems effectively integrate intermittent renewable resources and are regarded as an effective means to mitigate constraints of conventional fossil energy sources and environmental pollution. An ideal EES system meets the requirements of low cost, high safety, and rapid storage and release of large amounts of energy.[2] Compared with lithium, sodium exhibits higher abundance in the Earth's crust. Therefore, sodium-ion batteries (SIBs) are considered highly promising for EES applications.[3,4] The development of SIB cathode materials that combine low cost, high capacity, long cycle life, high power density, and adaptability to multifunctional applications receives increasing attention.[5] At present, layered transition metal oxides are affected by the Jahn–Teller effect, air instability, and oxygen loss, which make it difficult to achieve long cycle life and high rate.[6–8] Prussian blue and its analogues (PBAs) with high lattice water content generally exhibit poor structural stability during long term cycling.[9–11] By contrast, phosphate cathodes with stable three dimensional open frameworks show substantial potential for long cycle life and fast charge/discharge.[12,13]

$Na_3(VO_{1-x}PO_4)_2F_{1+2x}$ ($0 \leq x \leq 1$) is a member of the NASCION-type cathode family, attracting considerable interest owing to its high ionic conductivity, operating voltage, and energy density.[14–16] Among these, $Na_3V_2(PO_4)_2O_2F$ (NVPOF) stands out as one of the most promising sodium-ion battery (SIB) cathode candidates by virtue of its high theoretical specific capacity of 130 mA h g^{-1}. However, the fast Na^+ storage capability of NVPOF is hindered by poor reaction kinetics and low electronic conductivity.[17,18] It is well established that NVPOF is a mixed ionic–electronic conductor, in which Na^+ insertion/extraction is coupled with electron transfer (*i.e.*, redox reactions). At a low rate of 0.1C, the movement of ions and electrons stays fairly balanced, allowing the pristine NVPOF to achieve a high capacity (120 mA h g^{-1}).[20,21] In contrast, at high rate, electrochemical polarization—including ohmic, electrochemical, and concentration polarization—becomes significantly amplified. Issues such as current-dependent internal

[a]*School of Chemistry and Chemical Engineering, Guizhou University, Guiyang 550025, P. R. China. E-mail: aoxianquan@163.com; Li@gzu.edu.cn*

[b]*Guizhou Provincial Key Laboratory of Green Catalysis and Materials for Resource Conversion, Guiyang 550025, P. R. China*

[c]*College of Chemistry and Materials Engineering, Wenzhou University, Wenzhou, 325035, P. R. China. E-mail: xiaoyao@wzu.edu.cn*

[d]*School of Brewing Engineering, Moutai Institute, Renhuai 564501, P. R. China*

resistance drop (IR drop), interfacial charge-transfer limitation, and bulk ionic transport resistance severely restrict the enhancement of electrochemical performance. Increasing electronic conductivity can effectively mitigate IR drop and accelerate charge-transfer kinetics, while improving ionic conductivity facilitates bulk ionic transport. Therefore, simultaneous optimization of both electronic and ionic conductivities is essential to enhance the rate of NVPOF. Currently, conductive coatings have proven effective in boosting electronic conductivity but offer limited improvement in reaction kinetics.[18,22,23] Although morphological regulation enhances ion diffusion kinetics, its limited effect on intrinsic conductivity results in minimal improvement in high rate performance.[24,25] In contrast, appropriate element doping remains one of the most effective ways to simultaneously solve the problems of conductivity and kinetics. Current research on atom doping has mainly focused on Ti^{4+},[26] V^{3+},[27] Fe^{3+},[28] Mn^{2+},[29] Ni^{2+},[17] Mg^{2+},[30] Zn^{2+},[30] Y^{3+},[31] and high-entropy doping strategies.[19] Although many approaches achieve high capacities at low current densities, Na^+ storage performance at ultrahigh rates (≥20C) remains inadequate. In relevant reports on polyanion SIB cathodes, adjusting the local electronic structure of the matrix material can reduce the band gap and improve the intrinsic electronic conductivity.[32,33] In our previous study, Fe^{3+} ($3d^5$) enhanced the redox activity of the V^{3+}/V^{4+} couple and enabled multi electron reactions.[34] However, this advantage is accompanied by partial capacity loss at the high voltage plateaus (3.6 and 4.0 V). Consequently, achieving a balanced optimization of ionic and electronic conductivities in NVPOF cathodes remains essential to overcome the inherent limitations of high rate performance.

Herein, existing NVPOF optimization efforts target electronic or ionic transport in isolation; as a result, the overall electrochemical performance remains suboptimal. Inspired by reports that dopants with 3d orbitals can enhance intrinsic conductivity by modulating the local electronic structure, a transition metal/fluorine dual doping strategy was proposed to enhance both electronic and ionic conductivity simultaneously (Scheme 1). The introduction of elements with different spin states adjusted the spacing between the V $3d_{xz}$–O $2p_x$ bond and Fermi level, thereby improving the material's intrinsic conductivity. Meanwhile, the introduction of the F element effectively optimized the diffusion kinetics of Na^+. In particular, high spin Fe^{3+}/F^- dual doped $Na_3(VO)_{1.9}Fe_{0.1}(PO_4)_2F_{1.1}$ (NVPOF–Fe) delivers remarkable performance, achieving a specific capacity of 79.2 mA h g^{-1} and an energy density of 245 Wh kg^{-1} at 100C, while retaining 90.6% of its capacity after 2500 cycles at 20C. The assembled NVPOF–Fe‖HC full cell attains an energy density of 271.9 Wh kg^{-1} (based on the combined mass of the cathode and anode) and demonstrates outstanding cycling stability at 25 °C, 45 °C, and −20 °C. Notably, this work highlights the critical role of balanced enhancement of electronic and ionic conductivities in achieving high rate performance, offering a promising design principle for the development of advanced SIB cathodes.

Results and discussion

Considering that Sc^{3+} ($3d^0$), V^{3+} ($3d^2$), Cr^{3+} ($3d^3$), and Fe^{3+} ($3d^5$) possess distinct 3d orbital electron configurations, these cations were selected as dopants for pristine NVPOF. When M^{3+} (M = Sc, V, Cr, and Fe) substitutes for V^{4+}, charge neutrality was maintained by replacing dangling O^{2-} with F^-.[31,35] To meet the requirements of first-principles calculations for minor doping of Sc, V, Cr, and Fe, we established 2 × 1 × 1 supercells for NVPOF, NVPOF–Sc, NVPOF–V, NVPOF–Cr, and NVPOF–Fe, respectively, and verified the evolution of spin states in NVPOF and NVPOF–M (M = Sc, V, Cr, and Fe). Structural optimization revealed that heteroatom incorporation primarily induces lattice expansion along the *c* axis (Fig. S1). As shown in Fig. 1a and S2, the introduction of dopants invariably generated asymmetric spin configurations. Previous studies have shown

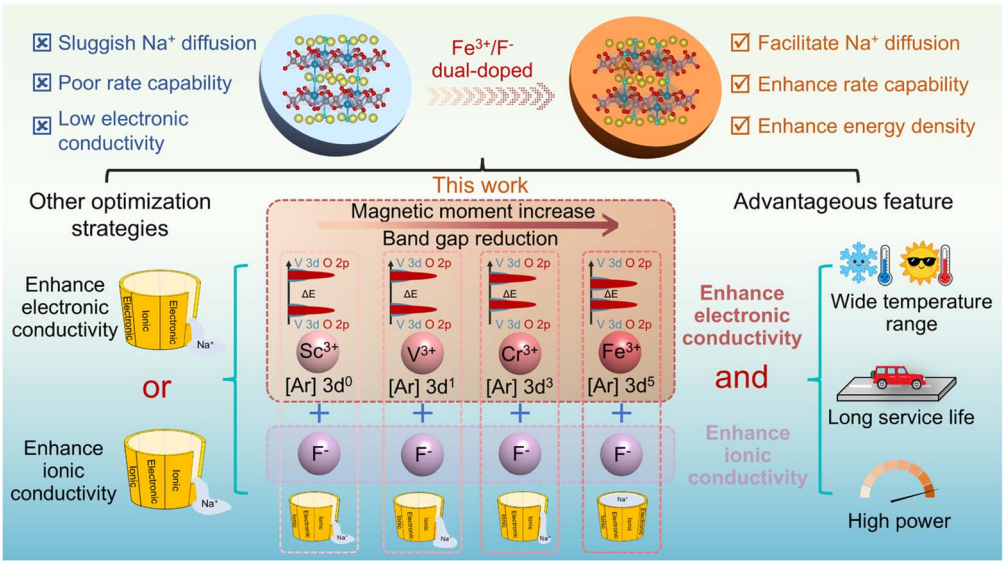

Scheme 1 Schematic diagrams of modification mechanisms for NVPOF–M (M = Sc, V, Cr, and Fe) cathodes.

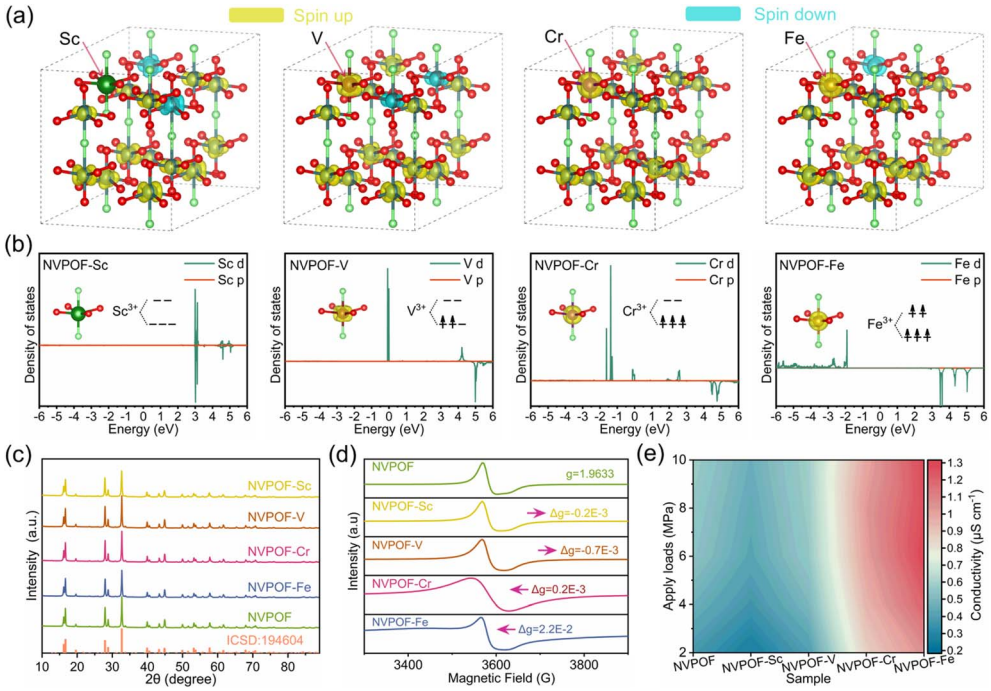

Fig. 1 Theoretical and structural characterization of NVPOF–M (M = Sc, V, Cr, and Fe) materials. (a) The comparative electronic spin states. (b) Projection density of states for Sc, V, Cr, and Fe elements. (c) XRD and (d) EPR spectra. (e) 2D contour plots of the four-point probe conductivity results of NVPOF–M (M = Sc, V, Cr, and Fe) and NVPOF under a load of 2–10 MPa.

that such configurations can effectively enhance vanadium redox activity.[36,37] Fig. 1b shows that Sc^{3+} exhibits a 3d orbital ($t_{2g}^0e_g^0$) without electron occupancy, while V^{3+} and Cr^{3+} are spin up $t_{2g}^2e_g^0$ and $t_{2g}^3e_g^0$ configurations, respectively, and Fe^{3+} is a high spin $t_{2g}^3e_g^2$ configuration.

NVPOF and NVPOF–M (M = Sc, V, Cr, and Fe) were further synthesized *via* a simple hydrothermal method. The XRD patterns (Fig. 1c) confirmed their high phase purity and crystallinity, its diffraction peak points towards the orthogonal crystal structure of NVPOF (ICSD no. 194604). The slight shifts of the (220) and (222) reflections toward lower angles confirm the successful incorporation of heteroatoms into the NVPOF lattice (Fig. S3). Owing to the comparatively large ionic radius of Sc^{3+}, NVPOF–Sc exhibits the greatest displacement among the doped samples.[38] To further elucidate the heteroatom-induced asymmetric electronic configurations of Sc^{3+}, V^{3+}, Cr^{3+}, and Fe^{3+}, Electron Paramagnetic Resonance (EPR) spectroscopy was performed (Fig. 1d). The *g* values decreased in the order NVPOF–Fe > NVPOF–Cr > NVPOF > NVPOF–Sc > NVPOF–V. Notably, NVPOF–V exhibited the smallest *g* value because the specific electron configuration of V^{3+} ($t_{2g}^2e_g^0$) renders it "EPR silent" under conventional perpendicular polarization mode. NVPOF–Fe showed a higher *g* value than NVPOF–Cr because high spin Fe^{3+} ($t_{2g}^3e_g^2$) has five unpaired electrons, significantly more than Cr^{3+} ($t_{2g}^3e_g^0$) with three unpaired electrons. These results confirm that Fe^{3+} doping increases the effective magnetic moment of the material. To better understand the contribution of heteroatom doping with different spin states to the conductivity, four point probe measurements were performed. Under loads of 2–10 MPa, NVPOF–Fe powders consistently exhibited the highest conductivity, followed by NVPOF–Cr (Fig. 1e). Furthermore, in conjunction with EPR spectroscopy, the electronic conductivity of NVPOF–M (M = Sc, V, Cr, and Fe) is found to be positively correlated with its effective magnetic moment. Higher load measurements (Fig. S4) further confirmed that NVPOF–Fe powders outperform all other compositions under any applied load. The superior conductivity is expected to mitigate ohmic polarization effects, thereby enhancing high rate electrochemical performance. Ionic conductivity measurements of NVPOF–M (M = Sc, V, Cr, and Fe) and pristine NVPOF reveal that heteroatom incorporation effectively reduces the bulk resistance (Fig. S5). Notably, NVPOF exhibits the highest bulk resistance, whereas NVPOF–Fe shows the lowest value, implying an enhanced ionic conductivity for NVPOF–Fe. Consequently, NVPOF–Fe and NVPOF–Cr are predicted to show improved performance at high rate.

Previous studies have shown that NVPOF can crystallize in two tetragonal symmetries, *I*4/*mmm* and $P4_2/mnm$, both featuring pseudo layered frameworks but differing in Na^+ distribution (Fig. 2a and b). To further elucidate the crystal structure, Rietveld refinements were performed on NVPOF–Fe based on both structures. The results indicate that NVPOF–Fe matches the $P4_2/mnm$ symmetry more closely (Fig. 2a). In the $P4_2/mnm$ framework, tetrahedral PO_4 groups and octahedral VO_5F units are interconnected *via* corner sharing, while pseudolayer pillars consist of two VO_5F octahedra linked through a shared F atom. Rietveld refinement was performed on the XRD patterns of NVPOF and NVPOF–M (M = Sc, V, Cr, and Fe) (Fig. S6 and Table S29). Given that the ionic radii of Sc^{3+}, V^{3+}, Cr^{3+}, and Fe^{3+} all exceed that of V^{4+},[38] the *c* axis length increased

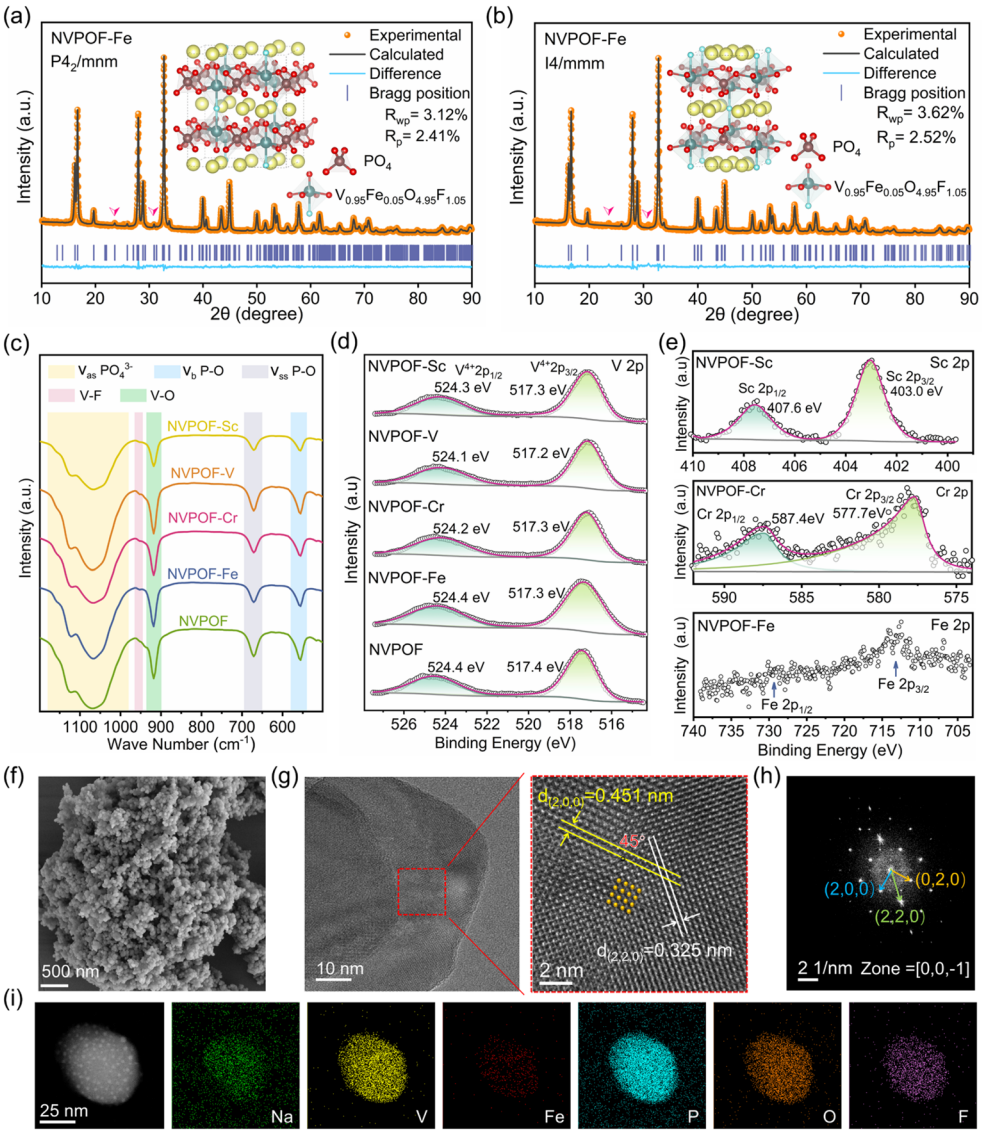

Fig. 2 Structural characterization of NVPOF–M (M = Sc, V, Cr, and Fe) materials. XRD Rietveld refinement patterns of NVPOF–Fe based on (a) $P4_2/mnm$ and (b) $I4/mmm$ crystal structures. (c) FTIR spectra. (d) High-resolution V 2p spectra, (e) high-resolution Sc, Cr, and Fe 2p spectra. (f) SEM image, (g) HRTEM image, (h) the FFT result of (g), and (i) EDS mapping of NVPOF–Fe.

upon doping, suggesting a widening of Na^+ diffusion channels. Fourier transform infrared (FTIR) spectroscopy is a powerful tool for probing the structure of NVPOF. As shown in Fig. 2c, the FTIR spectra of the five samples exhibit a broad absorption band in the range of 980–180 cm^{-1}, corresponding to the asymmetric stretching vibrations of PO_4^{3-} groups.[30,39] The symmetric stretching and bending vibrations of P–O bonds appear at 671 cm^{-1} and 555 cm^{-1}, respectively.[30,39] The vibration peaks at 895 cm^{-1} and 918 cm^{-1} can be attributed to V–F and V–O bonds, respectively.[30,39] X-ray photoelectron spectroscopy (XPS) measurements were carried out on NVPOF and NVPOF–M (M = Sc, V, Cr, and Fe) to determine the chemical states of the constituent ions. The full spectra clearly display the presence of Na, V, O, P, and F elements in all five samples (Fig. S7). The high-resolution V 2p spectrum displays distinct peaks at 517.3 and 524.0 eV, which are assigned to the V^{4+} $2p_{3/2}$ and V^{4+} $2p_{1/2}$ components, respectively (Fig. 2d).[30,39] The Sc 2p region can be deconvoluted into Sc^{3+} $2p_{3/2}$ and Sc^{3+} $2p_{1/2}$ peaks, indicating that scandium exists as Sc^{3+} (Fig. 2e).[40] The Cr 2p spectrum consists of Cr^{3+} $2p_{3/2}$ (577.7 eV) and Cr^{3+} $2p_{1/2}$ (587.4 eV) peaks, indicating that chromium exists in the form of Cr^{3+} (Fig. 2e).[41] Due to the low Fe concentration, only weak Fe $2p_{3/2}$ and Fe $2p_{1/2}$ signals can be identified (Fig. 2e). Combined with our previous findings, this indicates that Fe^{3+} ions do not undergo redox changes during the synthesis process.[34]

The morphological characteristics of NVPOF and NVPOF–M (M = Sc, V, Cr, and Fe) were further examined by scanning electron microscopy (SEM) and transmission electron microscopy (TEM). As shown in Fig. S8, all five materials are composed of nanoscale particles. TEM images indicate that all samples are formed by the aggregation of particles with a diameter close to 100 nm (Fig. S9–S12). High resolution TEM (HRTEM) images of

NVPOF–Fe and NVPOF particles show well-ordered lattice fringes with a single orientation (Fig. 2g and S12), indicating high crystallinity and a single-phase structure. In NVPOF–Fe, lattice spacings of 0.451 nm and 0.325 nm correspond to the (200) and (220) planes, respectively, with an interplanar angle of 45°. For NVPOF, the lattice spacing of 0.532 nm is indexed to the (002) plane. Fast Fourier transform (FFT) patterns obtained from HRTEM images reveal that NVPOF–Fe nanoparticles are single crystals exhibiting tetragonal symmetry (Fig. 2h). Energy dispersive X-ray spectroscopy (EDS) elemental mapping confirms the homogeneous distribution of all relevant elements across the nanoparticles (Fig. S9–S12).

The electrochemical performance of the five cathodes was evaluated in half cells using sodium metal as the anode. As shown in Fig. 3a and S13, at 0.5C, NVPOF–Sc, NVPOF–V, NVPOF–Cr, and NVPOF–Fe deliver discharge specific capacities of 135.8, 142.8, 133.3, and 139.8 mA h g^{-1}, respectively, all significantly higher than that of pristine NVPOF (121.4 mA h g^{-1}). During discharge, the specific capacities of NVPOF–V and NVPOF–Fe are 122.5 and 122.3 mA h g^{-1}, respectively, within the range of 4.3–3.4 V, far exceeding the 95.7 mA h g^{-1} of NVPOF, indicating better electrochemical activity of vanadium in these two cathodes. In addition, all cathodes deliver substantial capacity in the sloping region between 3.4 and 2.0 V, which may originate from interfacial storage and pseudocapacitive contributions.[42,43] The dQ/dV curve shows that the addition of Sc, V, Cr, or Fe leads to an increase in peak area and a decrease in potential shift of V^{4+}/V^{5+} redox pairs, indicating an increase in redox activity and a decrease in polarization (Fig. S14). Notably, NVPOF–Fe exhibits the smallest polarization, indicating superior reversibility (Fig. S14d). Polarization (IR drop) induced by ohmic resistance and electrochemical kinetics can significantly impair performance at high rate.[44,45] As depicted in Fig. 3b, all NVPOF–M (M = Sc, V, Cr, and Fe) electrodes show excellent specific capacities and energy densities. In particular, NVPOF–V and NVPOF–Fe deliver energy densities of 522.4 and 512.4 Wh kg^{-1} at 0.5C, respectively, which are far higher than that of pristine NVPOF. Given the higher redox activity of V^{3+} relative to Fe^{3+}, NVPOF–V accordingly exhibits the higher energy density. Both materials also outperform most sodium-ion battery cathodes reported to date (Table S1).

Fig. 3c presents the rate capabilities of NVPOF and NVPOF–M (M = Sc, V, Cr, and Fe) over 0.5–100C. At 0.5C, pristine NVPOF delivers a lower reversible capacity than all four doped counterparts. As the current density increases from 0.5 to 10C, the capacity advantage of the doped electrodes becomes increasingly evident. Upon further increasing the rate to 100C, NVPOF–Fe exhibits the largest capacity gain, followed by NVPOF–Cr. Specifically, at 100C the discharge capacities of NVPOF, NVPOF–Sc, NVPOF–V, NVPOF–Cr, and NVPOF–Fe are 25.4, 28.1, 26.2, 47.6, and 80 mA h g^{-1} (Fig. 3c and d), respectively. Correspondingly, the capacity retention of NVPOF at 100C is only 20.9% (relative to 0.5C), whereas NVPOF–Fe achieves 56.7%. Fe content optimization further shows that NVPOF–2.5% Fe and NVPOF–7.5% Fe deliver 47.9 and 49.6 mA h g^{-1} at 100C, respectively (Fig. S15a). Different batches of NVPOF–Fe cathodes provide a discharge capacity of nearly 80 mA h g^{-1} at 100C (Fig. S15b). At high currents, the GCD profiles indicate that NVPOF–Fe exhibits a smaller IR drop and reduced polarization on the voltage plateaus (Fig. 3d and S16), which, together with conductivity measurements, indicates that enhanced electronic conductivity mitigates ohmic polarization and underpins the superior high rate performance. These findings demonstrate that doping with high spin Fe^{3+} is an effective strategy to boost the rate capability of NVPOF. Moreover, as shown in the capacity–rate plot (Fig. S17), NVPOF–Fe is more competitive than advanced NVPOF cathodes reported to date (Table S10), particularly at high rate around and above 20C.

Fig. 3e, S18 and 3g present the cycling performance of NVPOF and NVPOF–M (M = Sc, V, Cr, and Fe) cathodes at rates of 5C, 10C, and 20C. Notably, NVPOF–Fe exhibits exceptional cycling stability across all three rates. At 5C, NVPOF–Fe delivers a maximum discharge capacity of 132.4 mA h g^{-1}, retaining 128.4 mA h g^{-1} after 600 cycles (Fig. 3e and f), corresponding to a capacity retention of 97.0%, or a per cycle fading rate of only 0.005%, markedly outperforming the other cathodes. In comparison, the retention values for NVPOF, NVPOF–Sc, NVPOF–V, and NVPOF–Cr are 87.3%, 93.2%, 90.5%, and 95.7%, respectively. The Fe doped NVPOF–2.5% Fe and NVPOF–7.5% Fe cathodes achieve retentions of 94.1% and 93.8% (Fig. S18b). GCD profiles over various cycles reveal no significant voltage plateau decay for NVPOF–Fe (Fig. 3f). Impressively, NVPOF–Fe achieves 94.1% retention after 1100 cycles at 10C (Fig. S18a, c and d) and 90.6% after 2500 cycles at 20C (Fig. 3g, S18e and f). At such high rates, slight voltage plateau decreases occur due to rapid Na^+ insertion/extraction, yet the cycling performance still far surpasses that of the other six cathodes. To further assess the multifunctionality of NVPOF–Fe, cycling tests were conducted at −20 °C and 45 °C. The NVPOF–Fe cathode exhibits impressive capacity and cycling stability at −20 °C. Specifically, when conducting charge and discharge tests at 1C, it can provide an initial discharge capacity of 114.8 mA h g^{-1} and retain 89.7% capacity after 360 cycles (Fig. 3h and S19). Notably, the average coulombic efficiency remained as high as 99.9% throughout the entire cycling process (Fig. 3h). At 45 °C, NVPOF–Fe capacity retention reaches 94% of its initial capacity after 500 cycles at 2C, the average Coulomb efficiency is 98% (Fig. 3i and j). The primary limitation at low temperature is diffusion-controlled kinetics, which is manifested by aggravated polarization. By contrast, at elevated temperature, thermal decomposition of the sodium salt, solvent, and interphase films becomes dominant, leading to a reduced coulombic efficiency. Overall, the multifunctional performance of the NVPOF–Fe cathode highlights its enormous potential as high performance cathodes for SIBs. Table S10 compares the rate and cycling stability of NVPOF–Fe with other leading analogues. Fig. 3k presents the Ragone plot comparing NVPOF–M (M = Sc, V, Cr, and Fe) cathodes with other advanced SIB cathodes. Among various reported sodium vanadium fluorophosphate oxides,[21,46] polyphosphates,[37,47,48] pyrophosphates,[49] and sodium vanadium fluorophosphates,[33] NVPOF–Fe delivers the most balanced and superior overall performance. Notably, at high power densities of approximately 5000 and 14 000 W kg^{-1},

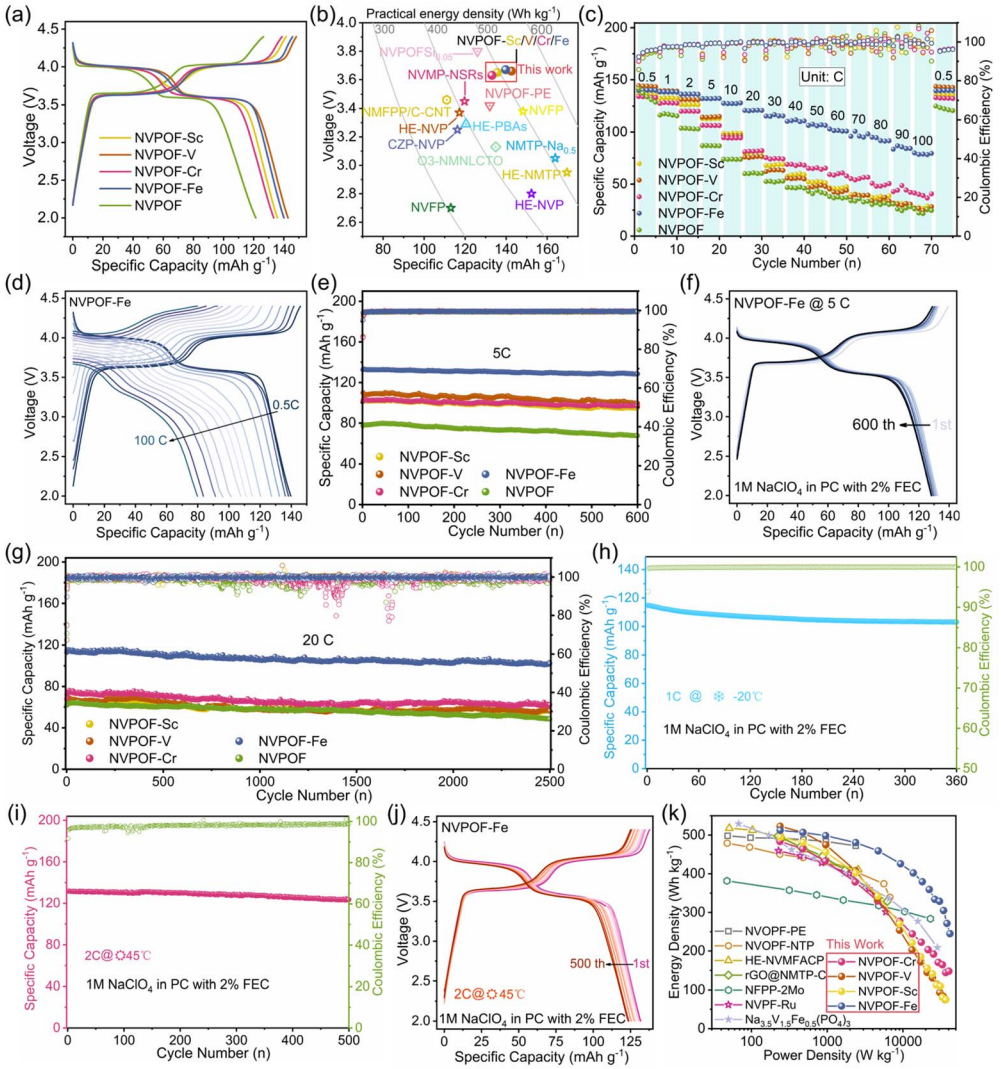

Fig. 3 The electrochemical performance of NVPOF and NVPOF–M (M = Sc, V, Cr, and Fe) cathodes. (a) Capacity comparison between NVPOF and NVPOF–M (M = Sc, V, Cr, and Fe) at 0.5C. (b) Comparison of operating voltage, specific capacity, and energy density of reported SIB half cells. (c) Rate performance. (d) GCD curves of NVPOF–Fe at different rates. The cycling performances at (e) 5C and (g) 20C, respectively. (f) GCD curves of NVPOF–Fe cathode at 5C. (h) The cycling performance of NVPOF–Fe at 1C and −20 °C. (i) The cycling performance and (j) GCD curves of NVPOF–Fe at 2C and 45 °C. (k) The Ragone plots of various advanced cathodes for SIBs.

NVPOF–Fe achieves energy densities exceeding 459 and 400 Wh kg^{-1}, respectively, demonstrating excellent compatibility between high energy and high power output.

To explore the differences in Na storage at different charge and discharge rates, we compared the voltage profiles of NVPOF and NVPOF–M (M = Sc, V, Cr, and Fe) at 0.5, 2, and 5C (Fig. 4a and S20). At 0.5C, compared to NVPOF–M, NVPOF exhibits significant voltage hysteresis in both regions A (3.75–3.95 V) and B (3.85–3.65 V) (Fig. S20a). The limited plateau capacity of NVPOF causes a premature transition to the next voltage plateau during charge/discharge, resulting in pronounced voltage hysteresis. This behavior stems from the insufficient redox activity of vanadium in the NVPOF cathode. Upon increasing the current density to 5C (Fig. 4a), the disparity in plateau capacity further enlarges, thereby producing voltage hysteresis in regions A and B, which becomes more conspicuous. Notably, NVPOF–Fe maintains the smallest voltage hysteresis at high rate, attributable to its increased plateau capacity. Electrochemical kinetics were probed by the galvanostatic intermittent titration technique (GITT) to determine Na^+ diffusion coefficients for NVPOF and NVPOF–Fe (Fig. 4b). The average Na^+ diffusion coefficient of NVPOF–Fe during charge/discharge is 1.23×10^{-9} cm^2 s^{-1}, which is 2.2 times that of NVPOF (5.54×10^{-10} cm^2 s^{-1}). Within the V^{4+}/V^{5+} redox plateau (orange region) range, NVPOF–Fe exhibits a higher Na^+ diffusion coefficient, indicating excellent kinetics. Combined with voltage distribution analysis, it has been proven that iron doping activates the V^{4+}/V^{5+} redox pairs and improves the capacity.

Further quantitative analysis of the reaction kinetics of NVPOF and NVPOF–Fe cathodes was conducted using cyclic voltammetry (CV). The CV profiles of NVPOF–Fe recorded at

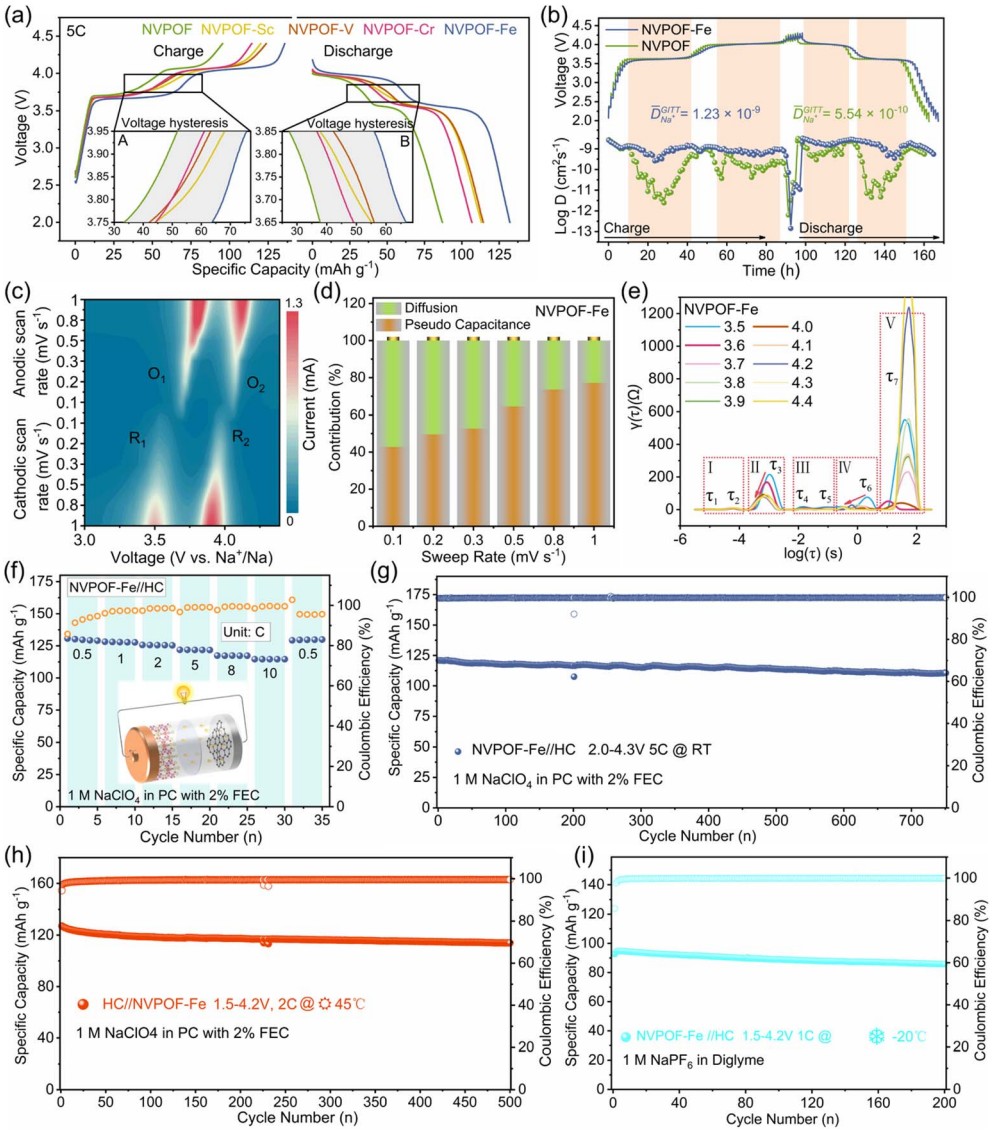

Fig. 4 (a) Voltage profiles of NVPOF and NVPOF–M (M = Sc, V, Cr, and Fe) cathodes at 5C (insets: the voltage hysteresis of the NVPOF cathode during the charge/discharge process). (b) GITT curves of NVPOF and NVPOF–Fe electrodes and the corresponding D_{Na^+} distributions. (c) The contour maps of CV curves of NVPOF–Fe at different scan rates. (d) Proportions of pseudocapacitive (orange area) and diffusion-controlled (green area) capacity of the NVPOF–Fe cathode at different scanning rates. (e) Distribution of relaxation time (DRT) obtained by deconvolution EIS. (f) The rate performance of NVPOF–Fe||HC full cell (inset: the schematic diagram of the NVPOF–Fe||HC full cell). (g) The cycling performance of the NVPOF–Fe||HC full cell at 5C and room temperature. (h) The cycling performance of the NVPOF–Fe||HC full cell at 2C and 45 °C. (i) The cycling performance of the NVPOF–Fe||HC full cell at 1C and −20 °C.

different scan rates (Fig. 4c) display two pairs of symmetric redox peaks. At a scan rate of 0.1 mV s^{-1}, the reduction peak R1 of NVPOF at 3.6 V is accompanied by a pronounced shoulder (Fig. S21a), indicative of side reactions; by contrast, NVPOF–Fe exhibits excellent reversibility (Fig. S22a). The *b* values derived from log(*i*) − log(*v*) analysis for NVPOF–Fe are 0.7703 and 0.7376 for the oxidation peaks (O1 and O2) and 0.8392 and 0.8154 for the reduction peaks (R1 and R2), respectively. Notably, the b values of O1, O2, and R2 exceed those of NVPOF (0.5969, 0.6826, and 0.7377). Since $b = 0.5$ corresponds to a diffusion controlled faradaic process and $b = 1$ to a pseudocapacitive process, values between 0.5 and 1 evidence the coexistence of diffusion control and pseudocapacitive charge storage (Fig. S21b and S22b).[50,51] At a scan rate of 0.8 mV s^{-1}, the pseudocapacitive contribution fraction was calculated (orange area /CV curve area) (Fig. S21c and S22c). Similar calculations were performed at different scan rates (Fig. 4d and S21d), revealing that Na^+ storage in the NVPOF–Fe cathode is predominantly diffusion controlled at low scan rates, but progressively shifts toward pseudocapacitive control as the scan rate increases; detailed results are summarized in Table S11. Unexpectedly, at high scan rates, NVPOF also exhibits a substantial pseudocapacitive fraction (Fig. S21d and Table S13). As is well known, particle downsizing is one of the most

effective approaches to enhancing pseudocapacitive contribution.[39] Therefore, we attribute the high pseudocapacitive fractions in both systems to their distinctive microstructural features.

Fig. S25a and b present the electrochemical impedance spectra (EIS) of NVPOF–Fe and NVPOF at different voltages, indicating that NVPOF–Fe possesses a smaller charge transfer resistance. As shown in Fig. 4e and S22c–e, compared with conventional EIS, the distribution of relaxation times (DRT) method effectively separates contact resistance (region I), ionic resistance (region II), surface electrochemical charge transfer (region IV), and solid state diffusion (region V).[52] Specifically, NVPOF–Fe exhibits lower contact resistance (region I), likely due to enhanced electronic conductivity induced by Fe doping. During the charge/discharge process, a thin and compact CEI (cathode electrolyte interphase) layer forms on the surface of the active material particles. This CEI not only effectively isolates the direct contact between the electrolyte and the material but also achieves a high ion diffusion rate, effectively preventing the continuous oxidation/decomposition of the electrolyte and excessive growth of the CEI layer. The lower resistances at τ_3, τ_4, and τ_5 suggest that NVPOF–Fe forms a thinner and more stable CEI layer. Furthermore, the parameter τ_6, which directly reflects the charge transfer resistance at the electrode surface, is markedly reduced upon Fe incorporation, especially in the 3.6–4.4 V range. Fe doping also optimized the Na^+ diffusion (τ_7) within the active material particles. Because redox reactions occur at ~3.6/4.0 V, electronic conductivity is increased and ionic conductivity is enhanced,[43] resulting in a pronounced drop in resistance for both NVPOF–Fe and NVPOF. Notably, at 3.6/4.0 V, NVPOF–Fe exhibits the lowest resistance among all samples, which can be attributed to improved electrical conductivity and Na^+ diffusion kinetics arising from Fe doping, consistent with the GITT results. Together with the measured electronic and ionic conductivities, these results confirm that NVPOF–Fe provides simultaneously enhanced electron and Na^+ transport. Collectively, the superior rate performance of NVPOF–Fe is attributed to Fe^{3+}/F^- incorporation, which concurrently improves electronic/ionic conductivity and thereby suppresses ohmic, electrochemical, and concentration polarization.

To evaluate the multifunctionality of NVPOF–Fe, a full cell (NVPOF–Fe‖HC) was assembled using NVPOF–Fe as the cathode and commercial hard carbon (HC) as the anode (Fig. 4f, inset). As shown in Fig. S24, owing to the low initial coulombic efficiency of HC, a presodiation treatment was applied prior to cell assembly (SI Experimental section). The NVPOF–Fe‖HC mass ratio was designed based on the capacity ratio at 1.3 A g^{-1}. Therefore, the N/P capacity ratio is 1.1 at 1.3 A g^{-1}, and the N/P mass ratio is 0.62 (Fig. S25). Fig. 4g presents the rate performance of NVPOF–Fe and HC in half cell configurations. Within the voltage range of 2.0–4.3 V, the NVPOF–Fe‖HC full cell delivers a reversible capacity of 129.0 mA h g^{-1} at 0.5C and retains 114.6 mA h g^{-1} at a high rate of 10C (Fig. 4f and S26a). Remarkably, based on the combined mass of the cathode and anode, the full cell achieves energy densities of 271.9 and 229.2 Wh kg^{-1} at 0.5C and 10C, respectively. At 5C and 25 °C, the full cell can provide an initial capacity of 120.9 mA h g^{-1}, and after 750 cycles, it still has 91.5% capacity (Fig. 4g and S26b). To further explore multifunctionality, high and low temperature cycling was performed over 1.5–4.2 V. At 2C and 45 °C, the capacity retention remains 89.6% after more than 500 cycles (Fig. 4h and S26c). Low-temperature (−20 °C) cycling tests were further conducted on the full cell using a diethylene glycol dimethyl ether-based electrolyte (1 M $NaPF_6$ in diglyme). The full cell retains 92.6% capacity after 200 cycles at 1C (Fig. 4i and S26d). Notably, the average coulombic efficiencies during long cycling at 25 °C, 45 °C, and −20 °C are 99.8%, 99.8%, and 99.4%, respectively. These results demonstrate excellent electrochemical performance under varied temperature conditions, highlighting the multifunctionality and practical potential of NVPOF–Fe as a cathode material.

The structural evolution of the NVPOF–Fe cathode during cycling was monitored by *in situ* X-ray diffraction (XRD) (Fig. S27a). Fig. 5a, c and S28b display the evolution of diffraction peaks. As shown in Fig. 5a, c and S27b, the characteristic reflections evolve systematically throughout cycling. In the charging process, the (111) diffraction peak gradually shifts to higher angles, while the (002) peak shifts to lower angles, ultimately converging at the end of charging. During the discharge process, both peaks show opposite trends. The (220)/(113) peaks exhibit similar behavior to (111)/(002), indicating a biphasic reaction mechanism, with the phase transition occurring in the transition region between the first and second voltage plateaus. The most intense diffraction peak, (222), shifts progressively toward higher angles during charging and fully recovers after discharge. It is worth noting that during Na^+ extraction, the (220) peak shifts to a higher angle, reflecting the continuous contraction of the *a*–*b* plane (Fig. 5c), which shortens the length of the O–V bond, typically resulting in bond energy. In contrast, the (002) peak shifts toward lower angles, indicating an elongation of the V–F bond, which corresponds to a reduction in bond energy. The Rietveld refinement results of the *in situ* XRD pattern indicate that the *a*/*b* lattice parameter shrinks by 2.2%, the c parameter expands by 2.3%, and the cell volume decreases by 2.2% (Fig. 5b). Despite cycling within a wide potential window of 2.0–4.3 V, such a small volume strain may be the reason why NVPOF–Fe exhibits excellent cycling performance. To further assess structural stability, first principles crystal orbital Hamiltonian population (COHP) analysis was performed to examine the influence of Fe doping on V–F bonding. The −ICOHP value is defined as the integral of pCOHP from −10 eV to the Fermi level and reflects the bond strength. Compared with the V–F bond in NVPOF (−ICOHP = 0.8035), the V–F bond in NVPOF–Fe exhibits a larger −ICOHP value (0.9609) (Fig. S28), indicating enhanced bond strength. This result suggests that, despite the expansion along the *c* axis, NVPOF–Fe retains a more robust structural framework than NVPOF.

Ex situ ultraviolet-visible spectroscopy (UV-Vis), X-ray absorption near edge structure (XANES), and X-ray photoelectron spectroscopy (XPS) were further employed to elucidate the charge compensation mechanism during the charge/discharge process. In the *ex situ* UV-Vis spectra, the maximum absorption band at 765 nm and the shoulder peak at 630 nm confirm

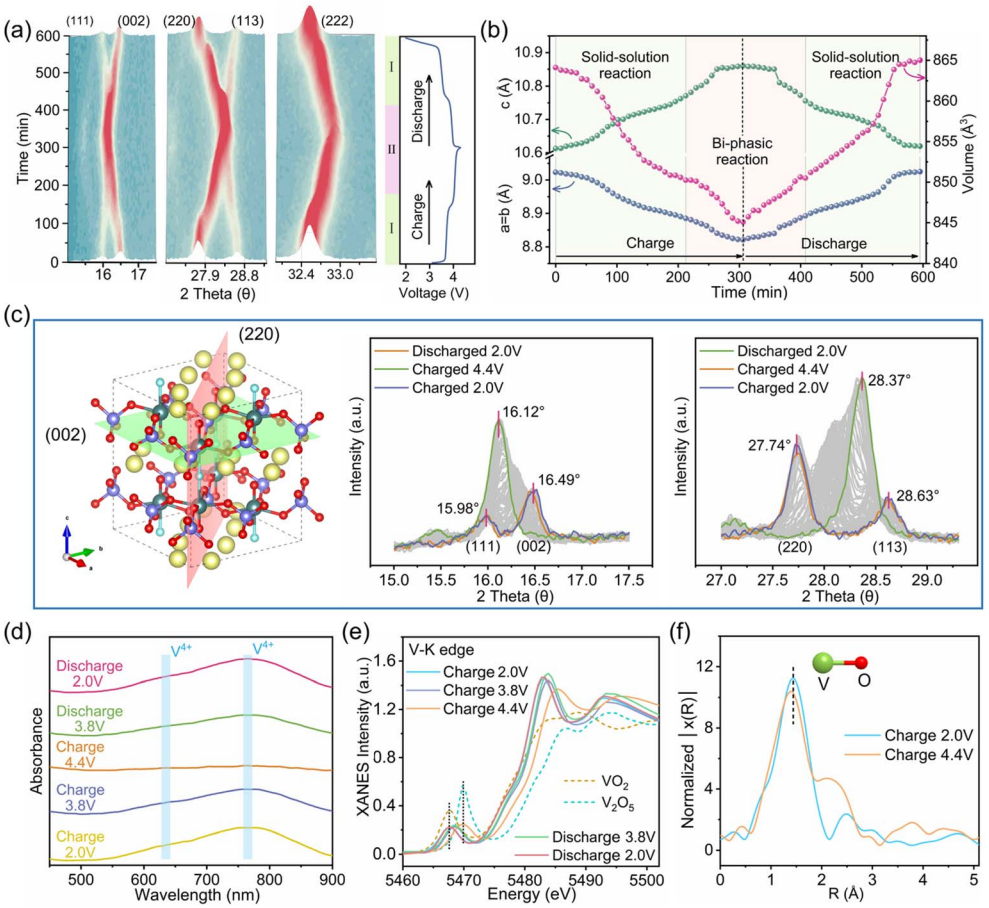

Fig. 5 (a) The 3D contour plot of *in situ* X-ray diffraction spectra of the (111), (002), (220), (113), and (222) diffraction peaks of the NVPOF–Fe cathode during the charging/discharging process was selected. (b) The changes in lattice parameters of the NVPOF–Fe cathode during the complete charge/discharge process. (c) *In situ* XRD patterns of the (002) and (222) diffraction peaks of the NVPOF–Fe cathode during the charging/discharging process. (d) FTIR spectra and (e) vanadium K-edge XANES spectra of the NVPOF–Fe cathode at different charge/discharge states. (f) EXAFS spectra of the NVPOF–Fe cathode at different charging states of the vanadium K-edge.

the reversibility of V^{4+}/V^{5+} redox pairs during the charging/discharging process (Fig. 5d). Fig. 5e displays the V–K edge XANES spectra at various states of charge. At 2.0 V, the pre-edge position coincides with that of standard VO_2. At 3.8 V, after extracting one mole of Na^+ from one mole of active material, the pre-edge positions gradually move towards higher energy. After the extraction of two moles of Na^+, the pre-edge aligns with that of standard V_2O_5. When discharged to 2.0 V, the V K-edge returns to its initial position, indicating that vanadium has a completely reversible oxidation state. Extended X-ray absorption fine structure (EXAFS) was employed to further probe interatomic distances in the NVPOF–Fe cathode (Fig. 5f). At 2.0 V, a prominent peak appears at a distance of approximately 1.5 Å, which can be attributed to the V–O bond.[26] After charging is completed, the peak slightly moves closer, indicating a subtle contraction of the V–O bond during sodium extraction. Fig. S29 shows high-resolution V 2p spectra at different charge/discharge states at 5C. The results confirmed that vanadium has higher redox activity in NVPOF–Fe at high rate.

Density functional theory (DFT) calculations were conducted to further investigate the impact of heteroatom doping on the electronic structure of NVPOF. Specifically, the charge density distribution along the (2–1 0) plane indicates that heteroatom incorporation alters the charge density between V and O (dangling) atoms (Fig. S30), The electron localization function (ELF) along the same plane (Fig. 6a) reveals that P–O bonds are covalent, V–O (dangling) bonds are polar covalent, and both O (in PO_4)–V and V–F bonds are ionic. Interestingly, heteroatom doping modifies the degree of extranuclear electron localization around V, producing asymmetric distributions. The charge differences for NVPOF–M (M = Sc, V, Cr, and Fe) show charge transfer following heteroatom substitution (Fig. S31), particularly V and O (dangling) atoms. Bader charge analysis for the five materials demonstrates that localized V atoms lose charge while non localized V atoms gain charge. Notably, dangling O atoms lose more charge than O (in PO_4) (Fig. S32).

To further assess how charge transfer affects the electronic structure, densities of states (DOSs) were computed for the five materials (Fig. 6b, e and S33a–c). Relative to pristine NVPOF, the band gaps of NVPOF–V, NVPOF–Sc, NVPOF–Cr, and NVPOF–Fe decrease progressively, indicating higher electronic conductivity in NVPOF–Fe (Fig. 6e), consistent with four probe

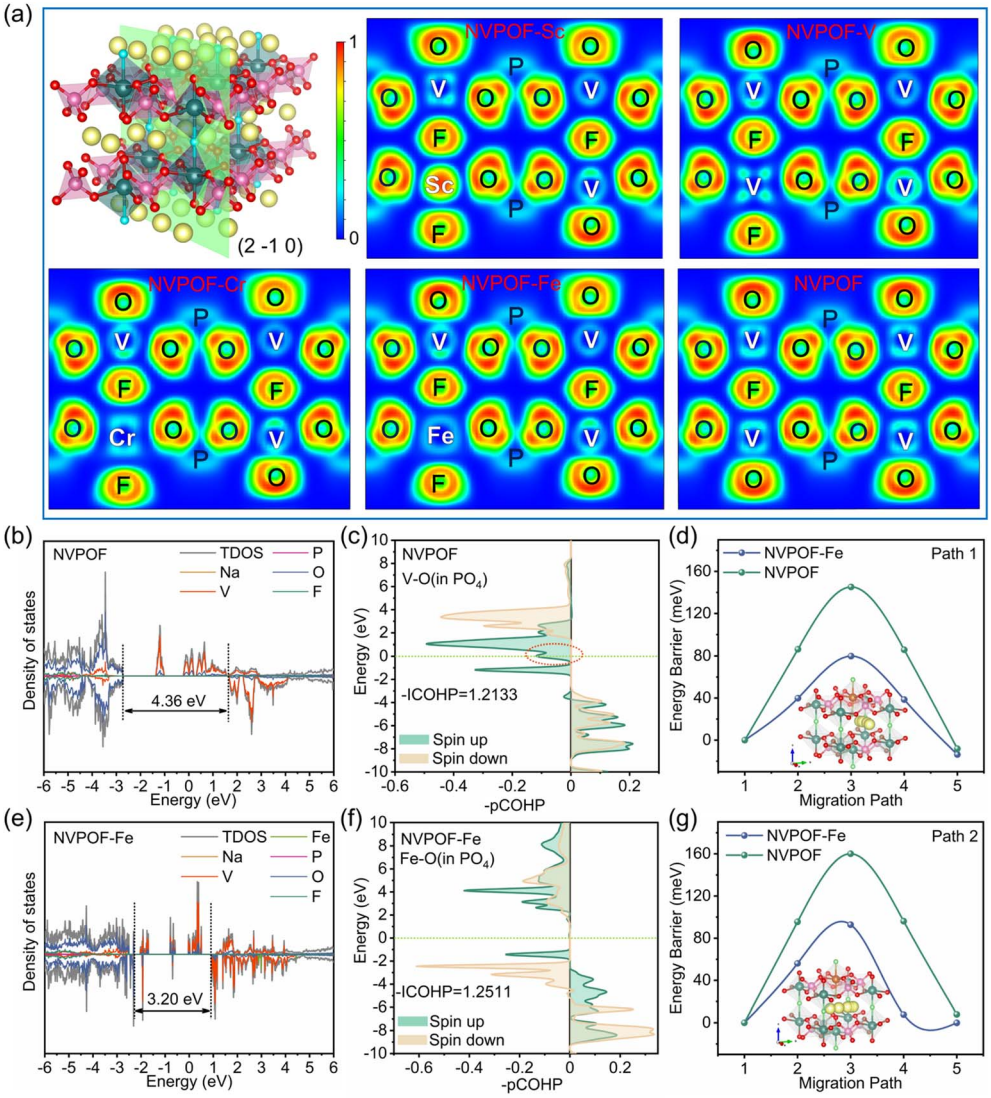

Fig. 6 (a) Electron Localization Function (ELF) calculation results. The density of states of (b) NVPOF and (e) NVPOF–Fe. COHP of (c) the V–O bond in NVPOF and (f) the Fe–O bond in NVPOF–Fe. Na^+ diffusion energy barriers for (d) P1 and (g) P2 pathways in NVPOF and NVPOF–Fe.

conductivity measurements. Local density of states (LDOS) analysis (Fig. S34) shows that in NVPOF, the valence band maximum (VBM) is dominated by O (in PO_4) 2p states, whereas the conduction band minimum (CBM) comprises O (dangling) 2p and V 3d states. By contrast, in the doped series NVPOF–M (M = Sc, V, Cr, and Fe), the VBM arises from the gain charge V1 3d orbitals together with O (dangling) 2p, while the CBM is contributed by the loss charge V2 3d and O (dangling) 2p orbitals. Orbital resolved analysis reveals close energy alignment between V $3d_{z^2}/3d_{xz}$ and O $2p_z/2p_x$, evidencing pronounced d–p hybridization: σ/σ* states form between V $3d_{z^2}$ and O $2p_z$, and π/π* states between V $3d_{xz}$ and O $2p_x$ (Fig. S35). In NVPOF–Fe, the VBM is governed by π bonding (V1 $3d_{xz}$–O $2p_x$) and the CBM by π* antibonding (V2 $3d_{xz}$–O $2p_x$). Crystal orbital Hamilton population (COHP) analysis indicates that in pristine NVPOF, the Fermi level falls within the π* antibonding region of V $3d_{xz}$–O $2p_x$ (Fig. 6c), with a similar feature for V–O (in PO_4), which reflects electronic instability.[53] In contrast, Fe doping modulates the valence electrons of V such that the Fermi level resides in an empty region. The integrated −ICOHP values (Fig. 6c and f) further demonstrate stronger covalency for Fe–O (in PO_4) in NVPOF–Fe than for V–O (in PO_4) in NVPOF, implying a more robust framework. Overall, high spin Fe^{3+} substitution for V^{4+} induces related electron redistribution: electrons transfer from localized V to O (dangling), raising the energy of π bonding states (V $3d_{xz}$–O $2p_x$), while non localized electrons transfer from terminal O to V, lowering the π* antibonding levels (Fig. S36). This dual shift narrows the band gap and accelerates electron transport.

It is well recognized that weakening Na–O bonding is conducive to Na^+ extraction.[54] Therefore, we conducted COHP analysis on Na–O (NVPOF), Na–O (NVPOF–Fe), and Na–F (NVPOF–Fe) bonds separately. Higher −ICOHP indicates stronger bond energy. Specifically, compared to Na–O (−ICOHP

= 0.0336) in NVPOF (Fig. S37a), doped Fe reduces the outer nuclear electrons of O (dangling), thereby reducing the strength of the Na–O (−ICOHP = 0.0208) bond (Fig. S37b). The Na–F (−ICOHP = 0.0312) bond in NVPOF–Fe is also lower than the Na–O bond in the original NVPOF (Fig. S37c), which further confirms that Fe^{3+}/F^{-} dual-doping is beneficial for the extraction of sodium ions. Further analysis was conducted on the migration energy barriers of sodium ions along the *a*-axis (path 1) and *b*-axis (path 2) migration paths near the dangling F atom. Compared to NVPOF (0.145 and 0.16 eV), NVPOF–Fe (0.08 and 0.093 eV) has a lower migration energy barrier (Fig. 6d and g). The substitution of terminal O by F is beneficial for the extraction of Na^{+}, which is consistent with the results of COHP analysis. Based on the observed high rate performance and four probe conductivity measurements, performance improvement can be achieved below 40C by adjusting diffusion kinetics alone, while above 40C, simultaneous enhancement of ion and electron transport is necessary.

Conclusions

In summary, Sc, V, Cr, and Fe were successfully incorporated into NVPOF *via* a simple hydrothermal synthesis. EPR and four point probe conductivity measurements revealed an increase in the material's effective magnetic moment alongside enhanced intrinsic electronic conductivity. Among these, Fe doped NVPOF (NVPOF–Fe) demonstrated outstanding electrochemical behaviour, delivering considerable specific capacity and energy density at 100C (80 mA h g^{-1}, 245 Wh kg^{-1}), together with a high capacity retention of 90.6% after 2500 cycles at 20C. *In situ* XRD monitoring during charge/discharge showed a minimal volume change of only 2.2% for the NVPOF–Fe cathode. *Ex situ* XANES/EXAFS and UV-Vis spectroscopy confirmed the reversible V^{4+}/V^{5+} redox behaviour in NVPOF–Fe throughout cycling. DFT calculations show that Fe doping regulates the distance between V $3d_{xz}$–O $2p_x$ and the Fermi level, effectively narrowing the bandgap and markedly accelerating interatomic electron transfer. In addition, F atoms were found to optimise the local Na^{+} diffusion kinetics, thereby enhancing ion storage capacity. This dual doping strategy achieves a balanced enhancement of both electronic and ionic conductivities. Therefore, the NVPOF–Fe||HC full cell exhibits excellent cycling stability at 25 °C, 45 °C, and −20 °C. More importantly, this doping strategy provides valuable guidance for the development of other high rate and long life cathode materials.

Author contributions

Qiang Fu: conceptualization, data curation, formal analysis, writing-original draft. Qin He: investigation, writing-original draft. Fangxiang Song: investigation, data curation, supervision. Xianquan Ao: conceptualization, project administration, funding acquisition, writing-review & editing. Hanxiao Liu: supervision, formal analysis. Yang Cao: data curation, supervision. Rong Li: conceptualization, supervision, project administration. Keliang Wang: investigation, formal analysis. Jing Li: formal analysis, project administration. Cuiqin Li: resources, formal analysis. Yao Xiao: conceptualization, supervision, visualization, formal analysis, writing-review & editing.

Conflicts of interest

There are no conflicts to declare.

Data availability

Essential data are fully provided in the main text and supplementary information (SI). Supplementary information is available. See DOI: https://doi.org/10.1039/d6sc00912c.

Acknowledgements

This work was supported by the Guizhou Science and Technology Platform Foundation (No. ZSYS [2025]-033), Natural Science Research Project of the Education Department of Guizhou Province (No. QJJ [2022] 001), Guizhou Provincial Science and Technology Program—Qian Ke He (Basic) (Grant No. QN [2025] 065), and Guizhou Provincial Science and Technology Program (Grant No. [2022] ZD006).

References

1 S. K. Nemomsa, N. D. Dejene, D. A. Efa, D. T. Negari, D. A. Ifa and D. H. Kumar, Clean energy demand in industry 4.0: trends, challenges, and opportunities, *Results Eng.*, 2025, 107260.
2 R. T. Yan and Q. Wang, Redox-Targeting-Based Flow Batteries for Large-Scale Energy Storage, *Adv. Mater.*, 2018, **30**, 1802406.
3 L. X. Han, S. X. Liao, S. H. Zhang, K. Chen, X. M. Chen, M. Y. Li, Q. Li, X. P. Ai, Y. L. Cao and Y. J. Fang, Unlocking electrochemical potential: amorphous NaFePO4 as a high-capacity and cycle-stable cathode material for advanced sodium-ion batteries, *Sci. China Mater.*, 2025, **68**, 1109–1116.
4 S.-Q. Su, Q.-C. Ling, Y.-J. Li, Y.-P. Yan, Y.-F. Zhu and Y. Xiao, Lattice-coherent interface-reinforced sodium-layered oxide cathodes, *Chem. Sci.*, 2025, **16**, 22852.
5 Z. Hong, Z.-C. Jian, Y.-F. Zhu, Y.-J. Li, Q.-C. Ling, H. Xin, D. Wang, C. Wu and Y. Xiao, Formulating cathode materials based on high-entropy strategies for sodium-ion batteries, *Chem. Sci.*, 2025, **16**, 17058.
6 H. Gao, J. Y. Li, F. Zhang, C. C. Li, J. Xiao, X. M. Nie, G. L. Zhang, Y. Xiao, D. Y. Zhang, X. Guo, Y. Wang, Y. M. Kang, G. X. Wang and H. Liu, Revealing the Potential and Challenges of High-Entropy Layered Cathodes for Sodium-Based Energy Storage, *Adv. Energy Mater.*, 2024, **14**, 2304529.
7 J. Xiao, H. Gao, Y. Xiao, S. J. Wang, C. Gong, Z. F. Huang, B. Sun, C. L. Dong, X. Guo, H. Liu and G. X. Wang, A hydro-stable and phase-transition-free P2-type cathode with superior cycling stability for high-voltage sodium-ion batteries, *Chem. Eng. J.*, 2025, **506**, 160010.
8 S. Wang, S. Chen, X. Liu, G. Feng, B. Zhang, W. Xing, Y. Xiao, H. Liu and W. Xiang, Revisiting high-valence dopant

mechanisms in Ni-rich cathodes: cation ordering dominates over morphological alignment for enhanced stability, *Chem. Sci.*, 2025, **17**, 3212.

9 Y. T. Gao, X. X. Wu, L. Wang, Y. F. Zhu, G. X. Sun, Y. X. Tang, M. Yan and Y. Z. Jiang, Structurally Stable, Low H_2O Prussian Blue Analogs toward High Performance Sodium Storage, *Adv. Funct. Mater.*, 2024, **34**, 2314860.

10 Y. Huang, X. Zhang, L. Ji, L. Wang, B. B. Xu, M. W. Shahzad, Y. X. Tang, Y. F. Zhu, M. Yan, G. X. Sun and Y. Z. Jiang, Boosting the sodium storage performance of Prussian blue analogs by single-crystal and high-entropy approach, *Energy Storage Mater.*, 2023, **58**, 1–8.

11 J. Peng, W. B. Hua, Z. Yang, J. Y. Li, J. S. Wang, Y. R. Liang, L. F. Zhao, W. H. Lai, X. Q. Wu, Z. X. Cheng, G. Peleckis, S. Indris, J. Z. Wang, H. K. Liu, S. X. Dou and S. L. Chou, Structural Engineering of Prussian Blue Analogues Enabling All-Climate and Ultralong Cycling Sodium-Ion Batteries, *ACS Nano*, 2024, **18**, 19854–19864.

12 Y. Y. Wang, Z. T. Cao, Z. Y. Du, X. X. Cao and S. Q. Liang, Research Progress of Iron-based Polyanionic Cathode Materials for Sodium-Ion Batteries, *Acta Phys.-Chim. Sin.*, 2025, **41**, 100035.

13 J. C. Xiao, J. T. Si, B. C. Pan and C. H. Chen, Revealing the Kinetic Limitation of $Na_7Fe_7(PO_4)_6F_3$ Polyanion Cathode with High Theoretical Capacity for Sodium-Ion Batteries, *Small*, 2025, **21**, 2412671.

14 R. H. Fang, J. Olchowka, C. Pablos, R. B. Nuernberg, L. Croguennec and S. Cassaignon, Impact of the F^- for O^{2-} Substitution in $Na_3V_2(PO_4)_2F_{3-y}O_y$ on Their Transport Properties and Electrochemical Performance, *ACS Appl. Energy Mater.*, 2022, **5**, 1065–1075.

15 S. Chakrabarty, T. Sharabani, S. Taragin, R. Yemini, A. Maddegalla, I. Perelshtein, A. Mukherjee and M. Noked, Boosting the capacity and stability of $Na_3V_2(PO_4)_2F_{3-2x}O_{2x}$ microspheres, using atomic layer deposition of artificial CEI, *J. Energy Storage*, 2024, **84**, 111507.

16 Q. X. Hu, M. J. Sun, Y. C. Zha, G. Q. Zhao, H. L. Tang, L. Yang, M. Yang, B. H. Pang, Y. J. Sun and H. Guo, Ti Substitution Strategy Improves Electrochemical Performance of $Na_3V_2(PO_4)_2F_3$ Cathode, *ACS Energy Lett.*, 2025, **10**, 1840–1850.

17 R. Essehli, H. Ben Yahia, R. Amin, M. Y. Li, D. Morales, S. G. Greenbaum, A. Abouimrane, A. Parejiya, A. Mahmoud, K. Boulahya, M. Dixit and I. Belharouak, Sodium Rich Vanadium Oxy-Fluorophosphate - $Na_{3.2}Ni_{0.2}V_{1.8}(PO_4)_2F_2O$ - as Advanced Cathode for Sodium Ion Batteries, *Adv. Sci.*, 2023, **10**, 2301091.

18 K. D. Gao, Q. Hu, G. M. Han, Y. Xia, J. Y. Liao and J. F. Yao, Polyaniline lamellated $Na_3V_2(PO_4)_2O_2F$ with fast kinetics toward high-performance sodium-ion batteries, *Chem. Eng. J.*, 2025, **511**, 162163.

19 G. S. Su, Y. J. Wang, J. W. Mu, Y. F. Ren, P. Yue, W. X. Ji, L. W. Liang, L. R. Hou, M. Chen and C. Z. Yuan, Insights into Tiny High-Entropy Doping Promising Efficient Sodium Storage of $Na_3V_2(PO_4)_2O_2F$ toward Sodium-Ion Batteries, *Adv. Energy Mater.*, 2025, **15**, 2403282.

20 X. Shen, Q. Zhou, M. Han, X. G. Qi, B. Li, Q. Q. Zhang, J. M. Zhao, C. Yang, H. Z. Liu and Y. S. Hu, Rapid mechanochemical synthesis of polyanionic cathode with improved electrochemical performance for Na-ion batteries, *Nat. Commun.*, 2021, **12**, 2848.

21 C. L. Xu, Q. Fu, W. B. Hua, Z. Chen, Q. H. Zhang, Y. Bai, C. Yang, J. M. Zhao and Y. S. Hu, Overcoming Kinetic Limitations of Polyanionic Cathode toward High-Performance Na-Ion Batteries, *ACS Nano*, 2024, **18**, 18758–18768.

22 X. Y. Li, S. L. Jiang, S. Y. Li, J. Y. Yao, Y. Zhao, T. Bashir, S. W. Zhou, S. Q. Yang, W. Y. Li, W. H. Zhu, T. T. Liu, J. Q. Zhao and L. J. Gao, Overcoming the rate-determining kinetics of the $Na_3V_2O_2(PO_4)_2F$ cathode for ultrafast sodium storage by heterostructured dual-carbon decoration, *J. Mater. Chem. A*, 2021, **9**, 11827–11838.

23 L. L. Zhang, J. Liu, C. Wei, P. P. Sun, L. Gao, X. K. Ding, G. Liang, X. L. Yang and Y. H. Huang, N/P-Dual-Doped Carbon-Coated $Na_3V_2(PO_4)_2O_2F$ Microspheres as a High-Performance Cathode Material for Sodium-Ion Batteries, *ACS Appl. Mater. Interfaces*, 2020, **12**, 3670–3680.

24 Z. Y. Gu, J. Z. Guo, Y. Yang, H. Y. Yu, X. T. Xi, X. X. Zhao, H. Y. Guan, X. Y. He and X. L. Wu, Precisely controlled preparation of an advanced $Na_3V_2(PO_4)_2O_2F$ cathode material for sodium ion batteries: the optimization of electrochemical properties and electrode kinetics, *Inorg. Chem. Front.*, 2019, **6**, 988–995.

25 S. Q. Li, X. Y. Lu, Y. Li, H. Z. Wang, Y. F. Sun, Q. N. Zhou, J. S. Yue, R. Q. Guo, F. Wu, C. Wu and Y. Bai, Dynamic Lock-And-Release Mechanism Enables Reduced ΔG at Low Temperatures for High-Performance Polyanionic Cathode in Sodium-Ion Batteries, *Adv. Mater.*, 2024, **36**, 2413013.

26 Y. R. Qi, W. Gao, H. Wang, D. Y. Liu, J. H. Deng, B. S. Guo, S. J. Bao and M. W. Xu, $Na_3(TiOPO_4)_2F$ microspheres as a long-life anode for Na-ion batteries, *Chem. Eng. J.*, 2020, **402**, 126118.

27 J. R. He, T. Tao, F. Yang and Z. P. Sun, Optimizing the Electrolyte Systems for $Na_3(VO_{1-x}PO_4)_2F_{1+2x}$ $(0\leq x\leq 1)$ Cathode and Understanding their Interfacial Chemistries Towards High-Rate Sodium-Ion Batteries, *ChemSusChem*, 2022, **15**, e202102522.

28 L. J. Yue, C. Peng, C. L. Guo, X. Y. Zhou, G. Li, N. N. Wang, J. S. Zhang, J. Q. Liu, Z. C. Bai and X. S. Zhao, $Na_3V_{2-x}Fe_x(PO_4)_2O_2F$: An advanced cathode material with ultra-high stability for superior sodium storage, *Chem. Eng. J.*, 2022, **441**, 136132.

29 P. Du, K. Mi, F. D. Hu, X. L. Jiang and X. W. Zheng, Mn-Doped Hollow $Na_3V_2O_2(PO_4)_2F$ as a High Performance Cathode Material for Sodium Ion Batteries, *Eur. J. Inorg. Chem.*, 2021, **2021**, 1256–1262.

30 H. Yu, H. B. Jing, Y. Gao, X. M. Wang, Z. Y. Gu, L. S. Li, J. J. Wang, S. Y. Wang, X. L. Wu, W. H. Qi, Q. H. Liang and C. F. Du, Unlocking the Sodium Storage Potential in Fluorophosphate Cathodes: Electrostatic Interaction Lowering Versus Structural Disordering, *Adv. Mater.*, 2025, **37**, 2400229.

31 V. Palomares, A. Iturrondobeitia, P. Sanchez-Fontecoba, D. Goonetilleke, N. Sharma, L. Lezama and T. Rojo, Iron-Doped Sodium-Vanadium Fluorophosphates: $Na_3V_{2-y}O_{2-y}Fe_y(PO_4)_2F_{1+y}$ (y < 0.3), *Inorg. Chem.*, 2020, **59**, 854–862.

32 H. Q. Huang, Y. F. Xia, Y. C. Hao, H. S. Li, M. Yousaf, S. Iqbal, H. G. Pan, M. Yan and Y. Z. Jiang, Local Electronic Structure Regulation Enabling Fluorophosphates Cathode with Improved Redox Potential and Reversible Capacity for Sodium-Ion Batteries, *J. Am. Chem. Soc.*, 2024, **146**, 28906–28913.

33 L. Wang, J. Q. Wang, H. H. Chen, H. H. Dong, H. C. Wang, Y. Wang, Y. Xiao, J. Wang and S. Q. Chen, Fast Screening Suitable Doping Transition Metals to $Na_3V_2(PO_4)_2F_3$ for Sodium-Ion Batteries with High Energy Density in Wide-Temperature Range, *Adv. Mater.*, 2025, **37**, 2505093.

34 Q. Fu, F. X. Song, C. H. Mu, Q. Q. Wu, K. L. Wang, S. Li and X. Q. Ao, Activating reversible multi-electron reaction of $Na_3(VO)_2(PO_4)_2F$ cathode via Fe/F dual-doping for high-energy and stable sodium storage, *Energy Storage Mater.*, 2025, **74**, 103960.

35 J. R. He, T. Tao, F. Yang and Z. P. Sun, Manipulating the Phase Compositions of $Na_3(VO_{1-x}PO_4)F_{1+2x}$ ($0 \leq x \leq 1$) and Their Synergistic Effects with Reduced Graphene Oxide toward High-Rate Sodium-Ion Batteries, *ACS Appl. Mater. Interfaces*, 2021, **13**, 60099–60114.

36 M. Z. Chen, W. B. Hua, J. Xiao, J. L. Zhang, V. W. H. Lau, M. H. Park, G. H. Lee, S. Lee, W. L. Wang, J. Peng, L. Fang, L. M. Zhou, C. K. Chang, Y. Yamauchi, S. L. Chou and Y. M. Kang, Activating a Multielectron Reaction of NASICON-Structured Cathodes toward High Energy Density for Sodium-Ion Batteries, *J. Am. Chem. Soc.*, 2021, **143**, 18091–18102.

37 Y. F. Zhou, G. F. Xu, J. D. Lin, Y. P. Zhang, G. Z. Fang, J. Zhou, X. X. Cao and S. Q. Liang, Reversible Multielectron Redox Chemistry in a NASICON-Type Cathode toward High-Energy-Density and Long-Life Sodium-Ion Full Batteries, *Adv. Mater.*, 2023, **35**, 2304428.

38 N. Agmon, Isoelectronic Theory for Cationic Radii, *J. Am. Chem. Soc.*, 2017, **139**, 15068–15073.

39 X. Y. Wang, Z. X. Sun, W. Lv, Z. H. Zhan, M. Huang, Q. Wang, F. Zhang, H. Wang and X. J. Liu, Advanced Multifunctional Sodium-Ion Battery with High Current Conversion, Long Cycle Life, and All-Climate Temperature Range by Dual-Multivalent Cation Doping Strategy, *Adv. Energy Mater.*, 2025, **15**, 2500471.

40 M. C. Biesinger, L. W. M. Lau, A. R. Gerson and R. S. C. Smart, Resolving surface chemical states in XPS analysis of first row transition metals, oxides and hydroxides: Sc, Ti, V, Cu and Zn, *Appl. Surf. Sci.*, 2010, **257**, 887–898.

41 X. L. Yi, H. Y. Luo, Y. M. Zhou, S. H. Feng, J. X. Wang, Z. X. Wang, J. G. Duan, D. Wang, H. J. Guo and G. C. Yan, Effect of Cr^{3+} doping on the electrochemical performance of $Na_3V_2(PO_4)_2F_3$/C cathode materials for sodium ion battery, *Electrochim. Acta*, 2023, **437**, 141491.

42 Z. H. Gan, J. Y. Yin, X. Xu, Y. H. Cheng and T. Yu, Nanostructure and Advanced Energy Storage: Elaborate Material Designs Lead to High-Rate Pseudocapacitive Ion Storage, *ACS Nano*, 2022, **16**, 5131–5152.

43 R. Usiskin and J. Maier, Interfacial Effects in Lithium and Sodium Batteries, *Adv. Energy Mater.*, 2021, **11**, 2001455.

44 C. F. Liu, Z. G. Neale and G. Z. Cao, Understanding electrochemical potentials of cathode materials in rechargeable batteries, *Mater. Today*, 2016, **19**, 109–123.

45 Y. Li, J. Tian, H. S. Yang, W. Liu and S. Q. Li, A concise analysis of cathode material degradation in sodium-ion batteries: insights from voltage hysteresis phenomena, *Mater. Sci. Eng., B*, 2025, **321**, 118460.

46 J. Z. Guo, P. F. Wang, X. L. Wu, X. H. Zhang, Q. Y. Yan, H. Chen, J. P. Zhang and Y. G. Guo, High-Energy/Power and Low-Temperature Cathode for Sodium-Ion Batteries: In Situ XRD Study and Superior Full-Cell Performance, *Adv. Mater.*, 2017, **29**, 1701968.

47 H. X. Li, M. Xu, C. H. Gao, W. Zhang, Z. A. Zhang, Y. Q. Lai and L. F. Jiao, Highly efficient, fast and reversible multi-electron reaction of $Na_3MnTi(PO_4)_3$ cathode for sodium-ion batteries, *Energy Storage Mater.*, 2020, **26**, 325–333.

48 C. Jin, Y. Wang, X. D. Zhao, J. T. Jin, Z. Y. Li, X. H. Qu, L. F. Jiao and Y. C. Liu, Entropy Driving "Quasi-Zero Strain" Stepwise Multicationic Redox Chemistry Toward a High-Performance NASICON-Cathode for Na-Ion Batteries, *Adv. Funct. Mater.*, 2025, **35**, 2422101.

49 W. S. Jian, L. Sun, J. Q. Gao, J. Y. Zeng, H. J. Wang, W. Y. Li, K. Wang, J. N. Huang, Y. He, J. H. Cao, L. M. Zhu, X. Y. Cao, W. T. Deng, G. Q. Zou, H. S. Hou and X. B. Ji, Valence-Modulated $Na_4Fe_3(PO_4)_2(P_2O_7)$ Cathode Tuned by Orbital-Delocalization for Extreme-Temperature Sodium Storage, *Angew. Chem., Int. Ed.*, 2025, e202514523.

50 C. Choi, D. S. Ashby, D. M. Butts, R. H. DeBlock, Q. L. Wei, J. Lau and B. Dunn, Achieving high energy density and high power density with pseudocapacitive materials, *Nat. Rev. Mater.*, 2020, **5**, 5–19.

51 Q. L. Wei, R. H. DeBlock, D. M. Butts, C. Choi and B. Dunn, Pseudocapacitive Vanadium-based Materials toward High-Rate Sodium-Ion Storage, *Energy Environ. Mater.*, 2020, **3**, 221–234.

52 D. Y. Semerukhin, A. V. Kubarkov, V. G. Sergeyev, O. A. Semenikhin and E. V. Antipov, Analysis of the Distribution of Relaxation Times (DRT) Responses of Li-Ion Cells as a Function of Their Preparation Conditions, *Electrochim. Acta*, 2024, **486**, 144092.

53 Y. S. Shi, F. S. Geng, Y. Sun, P. F. Jiang, W. H. Kan, W. Tong, X. Y. Lu, G. Y. Qian, N. Zhang, B. Wei, B. W. Hu, D. P. Cao and X. Lu, Sustainable Anionic Redox by Inhibiting Li Cross-Layer Migration in Na-Based Layered Oxide Cathodes, *Acs Nano*, 2024, **18**, 5609–5621.

54 J. Y. Zhou, X. Y. Li, X. L. Zhao, Y. W. Wang, E. R. Song and J. J. Liu, Rate and Cycling Performance of Ti and Cu Doped β-$NaMnO_2$ as Cathode of Sodium-ion Battery, *J. Inorg. Mater.*, 2024, **39**, 1404–1412.